Volume 14, Issue 2, 142418 (1-13)

Iranian Journal of Catalysis (IJC)

https://doi.org/10.57647/j.ijc.2024.1402.18

Visible-light Photocatalytic activity of Ag-Ce-ZnO/PANI and Ag-Ce ZnO/rGO novel nanocomposites: A comparative study

Marzieh Sadat Abdikhani, Fatemeh Sadat Seyed Atashi, Felora Heshmatpour*

Department of inorganic chemistry, Faculty of Chemistry, K.N. Toosi University of Technology, Tehran, Iran.

***Corresponding author:** heshmatpour@kntu.ac.ir

Review Paper

Received:
04 January 2024
Revised:
19 February 2024
Accepted:
01 May 2024
Published online:
11 May 2024

Abstract:

Ag, Ce co-doped ZnO-polyaniline (Ag-Ce/ZnO-PANI) and Ag, Ce co-doped ZnO-reduced graphene oxide (Ag-Ce/ZnO-rGO) were synthesized via precipitation and in-situ polymerization, an environmentally friendly process. Structural and optical properties were characterized using X-ray diffraction (XRD), Field Emission Scanning Electron Microscopy (FESEM), transmission electron microscopy (TEM), diffuse reflectance spectra (DRS), N_2 adsorption-desorption, photoluminescence spectra (PL), and Energy Dispersive X-ray analysis (EDX). The nanocomposites exhibited crystalline structures, with ZnO, metallic silver, and cubic crystalline CeO_2 identified in Ag-Ce-ZnO samples. Morphological studies revealed spherical shapes for ZnO and Ag-Ce-ZnO, while PANI displayed a fibrous structure. EDX confirmed elemental composition without impurities, and compositional mapping showed uniform dispersion. The photocatalytic degradation of Malachite green and para nitrophenol was performed using the nanocomposites under visible light irradiation. Among them, Ag-Ce/ZnO-rGO demonstrated significant photocatalytic efficiency, achieving 92% and 98% degradation of the organic contaminants, respectively. This enhanced activity can be attributed to increased specific surface area, efficient separation of photoinduced electron-hole pairs, enhanced dye adsorption, strong visible light absorption, and rapid transfer processes. Moreover, Ag-Ce/ZnO-rGO exhibited efficient reusability for five degradation cycles.

Keywords: Zinc Oxide; Polyaniline; Reduced graphene oxide; Photocatalysis; Visible light irradiation; Degradation

1. Introduction

In contemporary times, the utilization of nanocomposites to degrade organic compounds in water has become a crucial concern, capturing the attention of numerous scientists focusing on harnessing solar light. This method proves to be significantly more advantageous than alternative treatment approaches due to its heightened efficiency in the oxidation process and its economic properties. Moreover, the adoption of a green approach, exemplified by photocatalytic activity, is regarded favorably for being non-selective, operating at low temperatures, and presenting a non-energy-intensive option for neutralizing pollutant capabilities [1–4].
Numerous studies have been conducted on the mineralization of organic pollutants, leading to the introduction of ZnO as a robust nano compound with effective wastewater treatment properties. However, ZnO inertness in terms of visible light activity, attributed to its low surface area, wide bandgap, and rapid recombination of photodegradation excitons, poses a significant challenge in enhancing its photodegradation properties [5, 6].
The introduction of various impurities has resulted in the modification of the host metal ions' coordination environment within a given lattice. This alteration, by changing the bandgap structure, has the potential to enhance the photocatalytic ability. The insertion of foreign ions through the host lattice can lead to changes in the pristine structure, affecting

the mobility of charge carriers and yielding more favorable responses to incident photons. The number of dopants can either be above the valence band (VB) or below the conduction band (CB), capturing the photodegradation charge carriers. Subsequently, this process could exert influence on the redox pathway [7, 8]. Additional strategies have been employed to address ZnO's limited photodegradation ability under visible light irradiation. This involves combining it with a conjugated π-structure, such as conducting polymers, graphene, and similar materials.[9–11]. Materials with conjugated structures are utilized to ensure effective charge separation and to decrease the recombination rate of hole-electron pairs. [12]. Among various conducting polymers, polyaniline (PANI) presents several advantages, including cost-effectiveness, substantial visible-light absorption capability, a straightforward synthesis route, environmental stability, and high charge carrier mobility. [13, 14]. On the flip side, graphene can be considered carbon material with a two-dimensional conjugated chemical structure. It finds application in this field due to its substantial specific surface area, remarkable electron mobility, excellent electronic conductivity, good chemical stability, and promising photocatalytic potential [15, 16]. Numerous synthetic dyes are recognized as environmental pollutants, with Malachite Green (MG) standing out as a cationic tri-aryl methane dye extensively employed in food coloring, paper, leather, acrylic, silk, and wood industries, and even as a pesticide in aquaculture. However, the widespread use of MG in diverse applications has resulted in various issues concerning mammals, contributing to genotoxicity, cytotoxicity, carcinogenicity, and liver diseases [17]. Similarly, phenolic compounds are significant contaminants due to their disruptive impact on living organs, toxic nature, and their bio-recalcitrant characteristics. The release of these contaminants into the environment is primarily through wastewater generated by various industries, including tanning, different refineries, paint production, petroleum refining, pharmaceuticals, coke production, and more [18].

Thus, according to the studies on photocatalytic degradation, the requirement of removing wastewater from these newly synthesized compounds is affordable. So, the present research is focused on novel Ag- Ce- ZnO/PANI and Ag-Ce-ZnO/ rGO nanocomposites, and their photocatalytic activities in degrading MG and PNP (para nitrophenol) under visible light irradiation. The prepared compounds' reusability and stability were studied as well.

2. Experimental

2.1 Materials

Sodium hydroxide, zinc acetate dihydrate, silver nitrate, cerium acetate hydrate, ammonium peroxydisulfate (APS), graphite, potassium permanganate, hydrogen peroxide 30%, ethanol, sulfuric acid, phosphoric acid, hydrochloric acid, malachite green, and para nitrophenol were all bought from Merck. Although all these compounds were used as received without any more purification; aniline monomers were using two-time distillation.

2.2 Synthesis of zinc oxide and Ag, Ce co-doped ZnO

The synthesis of Pure ZnO and Ag, Ce co-doped ZnO (Ag-Ce-ZnO) nanocomposites were done through the precipitation strategy without any high temperature or pressure prerequisites, according to the procedure described in reference [8]. Specifically, pure ZnO was prepared by solving stoichiometric a sum of zinc acetate dihydrate in water (0.25 M, 100 mL), which served as the precursor solution in this study (solution1). In an isolated solution, dissolution of 2.5 g NaOH was done in 100 ml of ethanol/water (12.5%, v/v) (solution2). Both solutions were forcefully mixed for around 30 min. At that point, the considered NaOH solution was added to the zinc acetate dihydrate solution gradually. The obtained solution was blended at room temperature around 2 h to create a white color precipitate. The picked-up precipitate was at that point sifted by centrifuging and flushed with deionized water several times. At last, the obtained sample was dried for 12 h at the temperature of 60 °C. Finally, for crystallization, the calcination of the dried powder was done at the temperature of 450 °C for a period of 2 h; it was kept in a fixed holder for the following steps. The right sums of silver nitrate and cerium acetate dihydrate were included in the starting zinc acetate dihydrate solution to present Ag and Ce components to the ZnO nanoparticles. Meanwhile, the reaction conditions were the same. In the case of preparation, the use was made of Ag-Ce-ZnO, 0.22 g cerium acetate hydrate, and 0.04 g silver nitrate (2% molar Ce and 1% molar Ag relative to ZnO).

2.3 Synthesis of polyaniline (PANI)

0.9313 g of distilled aniline monomer was dissolved in 150 mL of the 0.01 M HCl solution in a sample experiment. Next, the mixture was sonicated for 45 minutes. 2.2 g of the APS oxidant was subjected to dissolution in 20 ml deionized water by the addition into the above solution in a drop-wise manner through gentle stirring. The reaction took place after 4 h with magnetic stirring; it was completed after 24 h. Finally, the generated greenish-black precipitate was collected and subjected to washing by applying deionized water and ethanol several times; then it was kept in the oven at the temperature of 60 °C for a period of 12 h.

2.4 Synthesis of graphene oxide (GO)

In this method, a mixture of H_2SO_4 and H_3PO_4 (360:40 mL) was added to the graphite flakes mixture (3 g) and $KMnO_4$ (18 g). The resulting black slurry was warmed up to 50 °C for a period of 24 h in magnetic stirring conditions. In the next step, the reaction vessel was subjected to cooling in some ice bath. The completion of the reaction was done with the addition of deionized ice (400 mL) into the solution and H_2O_2 30% by shaking so that the suspension color was changed to a yellowish one, and the release of the bubble was stopped (10 mL). The provided compound was filtrated and washed with applying deionized water, HCl (5%), and ethanol three times, respectively. Then, drying was done in an oven at the temperature of 60 °C for a period of 12 h to remove the impurities.

2.5 Synthesis of Ag-Ce-ZnO/PANI nanocomposite

A typical in-situ polymerization strategy was applied for the aniline polymerization when Ag-Ce-ZnO nanoparticles were present. Sonication of Ag-Ce-ZnO nanoparticles (0.9313 g) was then done in some 150 mL aqueous solution including aniline monomer (0.01 mol) and hydrochloric acid (0.01 mol). Dissolution of the APS oxidant (0.01 mol) was done in 20 mL deionized water and then added to Ag-Ce-ZnO and aniline monomer by mixing. Polymerization proceeded for 12h within the ice bath (0-5°C). The nanocomposite of Ag-Ce-ZnO/PANI was collected as a precipitate by filtering. Filtrations of this residue were done; this was continued with washing by deionized water a few times; after that, it was dried at the temperature of 60 °C for 12 h.

2.6 Ag-Ce-ZnO/rGO nanocomposite Synthesis

Synthesis of Ag-Ce-ZnO/rGO nanocomposites was done using the hydrothermal method. Accordingly, 0.3 g Ag-Ce-ZnO was added to the GO solution (0.003 g GO, 15 ml ethanol, and 30 ml deionized water), and stirring was continued around 2 h to gain a homogeneous suspension. Then, the resulting suspension was sent to some 50 ml Teflon-lined stainless steel autoclave and kept at 120 °C for a period of 3 h to reduce GO and Ag-Ce-ZnO depositing. Eventually, cooling of the autoclave was done at room temperature. The providing nanocomposite was recovered by centrifuging; it was washed several times using ethanol and deionized water to remove any impurities dried in the oven at the temperature of 60 °C for a period of 12 h.

2.7 Characterization

The nanocomposite phase structure, as well as crystallite size, was estimated by the X-ray diffraction technique (XRD, Philips Export – MPD); this was done by utilizing Cu-Kα radiation with the 1.5439 $\AA$ wavelength. Field emission scanning electron microscopy (FESEM, S4160 Hitachi, Japan) was then employed to examine the microstructure and morphology of the samples equipped with energy-dispersive X-ray spectroscopy (EDS). The optical characteristics of the samples were analyzed by Ultraviolet-visible (UV-Vis) spectroscopy (Perkin Elmer Lambda 35) within the 200-800 nm range. The measurement of the specific surface area was done by nitrogen adsorption at the temperature of -195.8 °C according to the BET equation (Physisorption Analyzer, ASAP 2020, Micromeritics). Photoluminescence spectra (PL) for the as-prepared catalysts were investigated by a Hitachi F-7000 DC-0506 fluorescence spectrometer (PerkinElmer LS55, America) with an emission wavelength at 325 nm. The photocatalytic activity was also assessed by employing a UV-Vis spectroscopy.

2.8 Photocatalytic activity studies

The synthesized samples' photocatalytic properties were assessed by the degradation of MG and PNP under visible light irradiation conditions. The adsorption-desorption equilibrium before the photocatalytic test of the photocatalyst (25 mg) was allowed to be mixed with the MG/PNP solution (100 mL, 10 mg.L^{-1}); stirring was done in the dark for a period of 30 min. An Xe arc 300 W Oriel lamp served as the source of light. At some specific times, 3 mL of the reaction mixture, including the suspended photocatalyst solution, was obtained and centrifuging was done to abolish the photocatalyst. Then, it was analyzed by considering the 250-700 nm wavelength UV-Vis spectroscopy range. The concentration of MG and PNP was recognized by recording the supernatant's variation at 621 nm and 400 nm, respectively. At last, the samples' photocatalytic ability was computed by the following formula (Equation 1):

$$\%X = \left[\frac{C_0 - C}{C_0}\right] \times 100 \quad (1)$$

, where X is the photodegradation efficiency, and C_0 and C refer to the concentrations of the organic pollutants prior to and following light irradiation, respectively. The photocatalytic degradation activity's reproducibility on the samples was surveyed at 10 mgL^{-1} MG/PNP concentration and the 0.25 mgmL^{-1} catalyst dosage for each of the cycles. The catalysts recovered were subjected to washing by applying ethanol and deionized water. Then, drying was done in the air prior to reusing.

3. Results and discussion

3.1 X-ray diffraction

Fig. 1 represents the XRD patterns belonging to ZnO, Ag-Ce-ZnO, Ag-Ce-ZnO/PANI, and Ag-Ce-ZnO/rGO nanocomposites. Due to ZnO diffraction pattern, sample signals at 31.9°, 34.4°, 36.2°, 47.6°, 56.4°, 62.9°, 66.4°, 67.8°, 69.2°, 72.7° and 76.9° were attributed to the reflections (100), (002), (101), (102), (110), (10^3), (200), (112), (201), (004) and (202), respectively (Fig. 1a). Based on literature and the JCPDS no. 36-1451, all these diffractions were in a good agreement with the wurtzite crystal structure [19]. Fig. 1b shows the Ag-Ce-ZnO nanoparticles XRD patterns in comparison with ZnO and Ag-Ce-ZnO, thus indicating the additional diffraction peaks related to (111), (200), and (220) planes related to the face-centered cubic phase of metallic silver (JCPDS no. 00-004-0783) [20]. Also, the weak peak at 2θ=28.72° could be attributed to the (111) plane belonging to the cubic crystalline CeO_2 structure (JCPDS no. 81-0792) [21]. Besides, the existence of

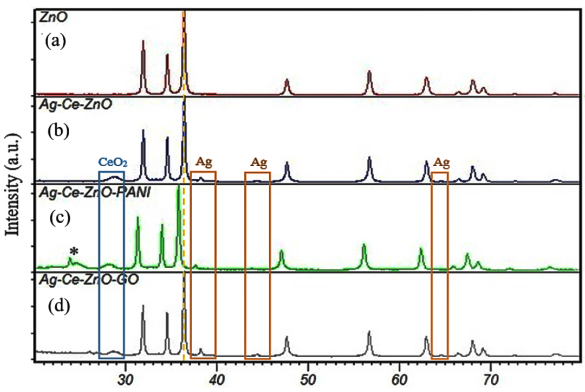

Figure 1. XRD patterns of (a) ZnO, (b) Ce-Ag-ZnO, (c) Ag-Ce-ZnO/PANI, and (d) Ag-Ce-ZnO-rGO.

sharp and intense peaks approved the crystallization of the fabricated nanopowders. According to Ag-Ce-ZnO/PANI samples, XRD peaks two sets could be attributed to Ag-Ce-ZnO and PANI, respectively (Fig. 1c); peaks which are indicated by asterisks (*) represent PANI. By considering the XRD patterns related to the Ag-Ce-ZnO-PANI nanocomposite and Ag-Ce-ZnO nanoparticles, they were found to be the same; only the additional broad diffraction peak appeared at around $2\theta = 25^{\circ}$, which corresponded to PANI (200) crystal planes [22]. Hence, the crystalline wurtzite structure of Ag-Ce-ZnO nanoparticles was not changed after the polymerizing by PANI molecules. The shifting of ZnO nanoparticle characteristic peaks to the lower angles was done by PANI composition. It indicated that the distance existing between diffraction lattice ZnO nanoparticles levels was gained by considering the addition of PANI chains among the crystalline plane spaces in the considered ZnO structure [23]. XRD patterns of Ag-Ce-ZnO-rGO are presented in Fig. 1d. There was no characteristic diffraction peak of GO in Ag-Ce-ZnO/rGO composite patterns. It showed that GO was reduced by the hydrothermal treatment to graphene and had good dispersion into the composites [24].

The crystallite size, of the sample has been estimated from the broadening of the XRD peaks using the Scherrer equation (Equation 1) with the size-strain plot shown in Fig. 2 [25]:

$$D = \frac{K\lambda}{\beta \cos\theta} \tag{2}$$

where λ is the X-ray wavelength, K is a structure constant, θ denotes the diffraction angle, β represents the full width at half maxima.

The size–strain plot also known as the W–H plot considers the effect of stress broadening on the nanostructure size and is calculated by using the Williamson–Hall method (Equation 3) [26]:

$$\beta = \frac{K\lambda}{D\cos\theta} + 4\varepsilon \sin\theta \tag{3}$$

where ε measures the stress coefficient and its value is measured from the slope of the fitted line. This stress broadening coefficient leads to an increase in grain size as compared to that measured by the Debye–Scherrer equation given in Table 1.

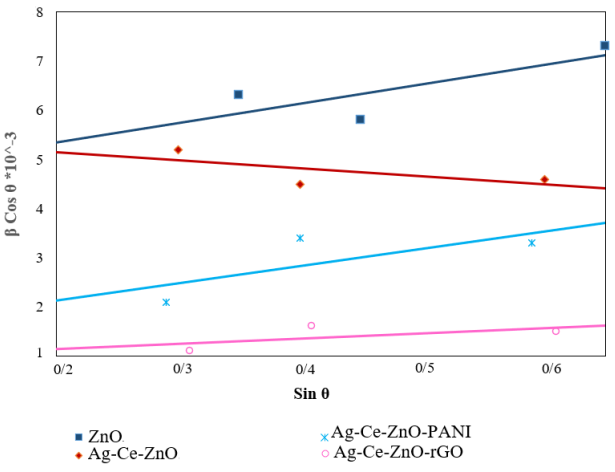

Figure 2. Williamson–Hall (W–H) plot of the samples ZnO, Ag-Ce-ZnO, Ag-Ce-ZnO/rGO , and Ag-Ce-ZnO/PANI.

3.2 FESEM

FESEM was applied to study the morphology of the nanostructures. The FESEM images of the ZnO, Ag-Ce-ZnO, PANI, Ag-Ce-ZnO-PANI, RGO, and Ag-Ce-ZnO-rGO samples are illustrated in Fig. 3(a-f). The ZnO and Ce-Ag-ZnO samples morphology showed a disordered spherical shape (Fig. 3a, b). From the micrographs, it is understandable that polyaniline (PANI) had a polyaniline fibrous and porous structure, whereas the ZnO nanoparticles covered the fibrous structure (Fig. 3c). Given the crystalline ZnO and the amorphous polymer, the morphology of the sample (Ag-Ce-ZnO/PANI) approved the coexistence of nanoparticles and ZnO's embedding nanoparticles in the polymer matrix (Fig. 3d). In any case, the composite led to Ag-Ce-ZnO/PANI composite, which was semi-crystalline. The ZnO spheral structure was disseminated inside the PANI matrix, and the bigger particles contributed to agglomeration [27]. Fig. 3e illuminates the smooth morphology of the reduced graphene oxide. So, the flaky texture surface of graphene was broken off in different directions, thus showing its layered structure. The Ag-Ce-ZnO/rGO FESEM image is represented in Fig. 3f. The FESEM images emphasized the ZnO anchoring on the graphene sheets' surface.

The Ag-Ce-ZnO/rGO and Ag-Ce-ZnO/PANI surface morphology were characterized using TEM analysis, as shown in Fig. 4a, b. It could be observed that Ag-Ce-ZnO was well distributed over the entire rGO surface (Fig. 4a). Besides, the nanocomposites clearly showed that the Ag-Ce-ZnO nanoparticles were embedded in the PANI matrix, as can be seen in Fig. 4b.

Fig. 5 presents the energy-dispersive X-ray spectra related to the PANI, Ag-Ce-ZnO/PANI, rGO, and Ag-Ce-ZnO/rGO. Zn, O, Ce, Ag, C, and N could be obviously seen in the EDX spectra. The EDX pattern verified that the samples had been successfully synthesized without any significant impurity. The compositional mapping was done for the created Ag-Ce-ZnO/PANI and Ag-Ce-ZnO/rGO samples to assess the elemental dissemination on the sample surface (Fig. 5). The Zn, O, Ce, Ag, C, and N elements had a uniform dispersion all through the surface.

The compositional mapping was done for the created Ag-Ce-ZnO/PANI and Ag-Ce-ZnO/rGO samples to assess the elemental dissemination on the sample surface (Fig. 6). The Zn, O, Ce, Ag, C, and N elements had a uniform dispersion

Table 1. Average Crystallite size of the samples of ZnO, Ag-Ce-ZnO, Ag-Ce-ZnO-PANI, and Ag-Ce-ZnO-rGO.

sample	average crystallite size (nm)	
	Debye–Scherrer	Williamson–Hall
ZnO	43.54	45.21
Ag-Ce-ZnO	59.32	60.85
Ag-Ce-ZnO-PANI	75.65	77.14
Ag-Ce-ZnO-rGO	86.15	89.59

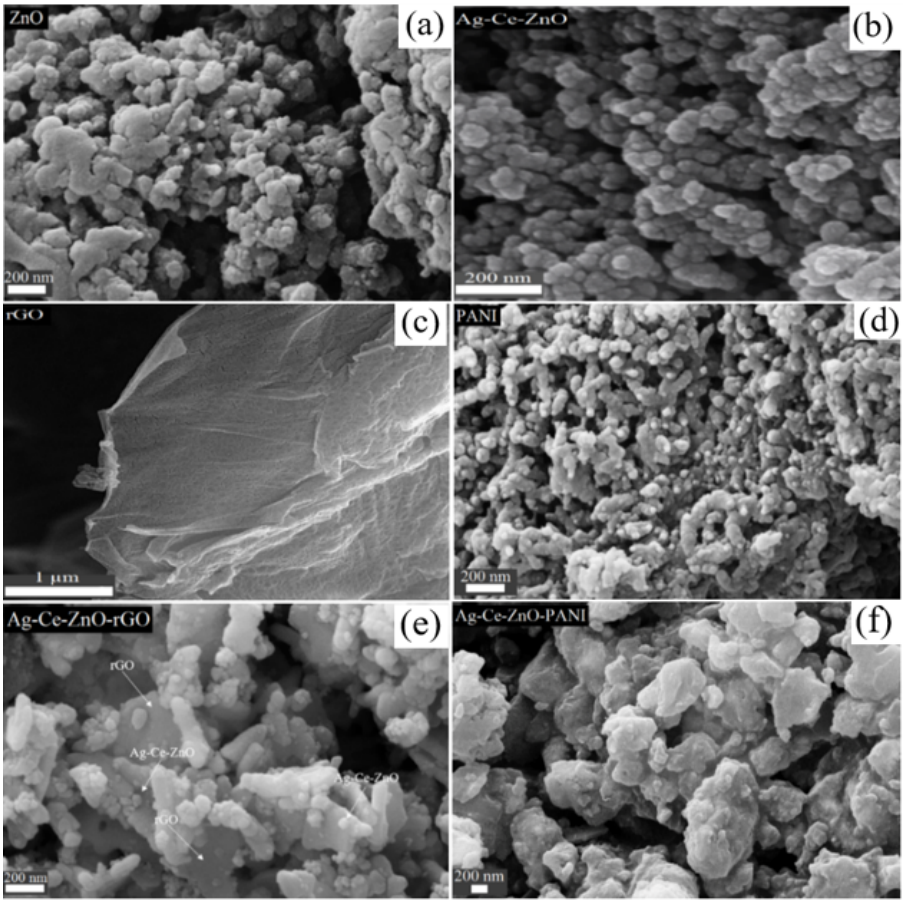

Figure 3. FESEM image related to (a) ZnO, (b) Ag-Ce-ZnO, (c) rGO, (d) PANI, (e) Ag-Ce-ZnO-rGO and (f) Ag-Ce-ZnO-PANI samples.

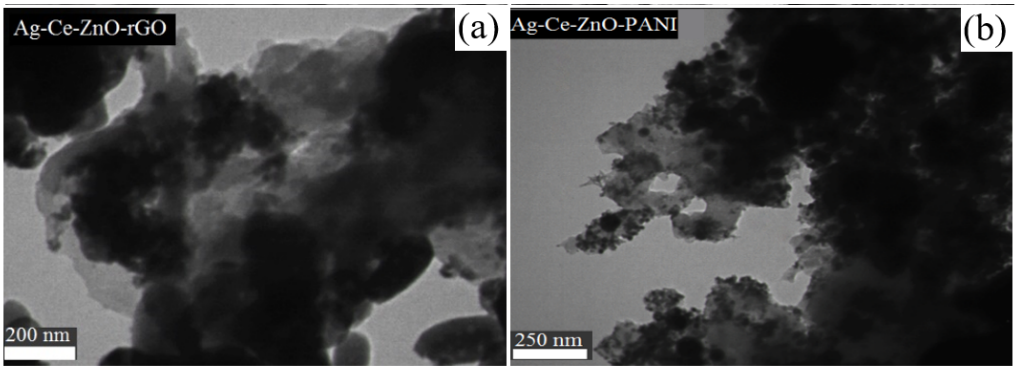

Figure 4. TEM image of the (a) Ag-Ce-ZnO-rGO and (b) Ag-Ce-ZnO-PANI samples.

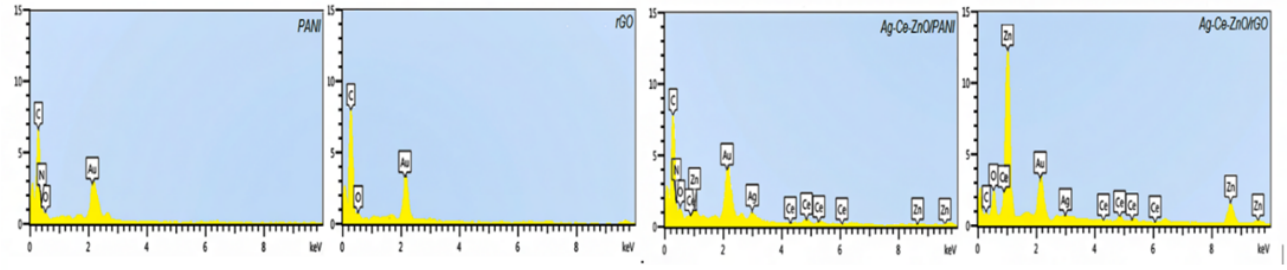

Figure 5. EDX analysis of PANI, rGO, Ag-Ce-ZnO/PANI and Ag-Ce-ZnO/rGO.

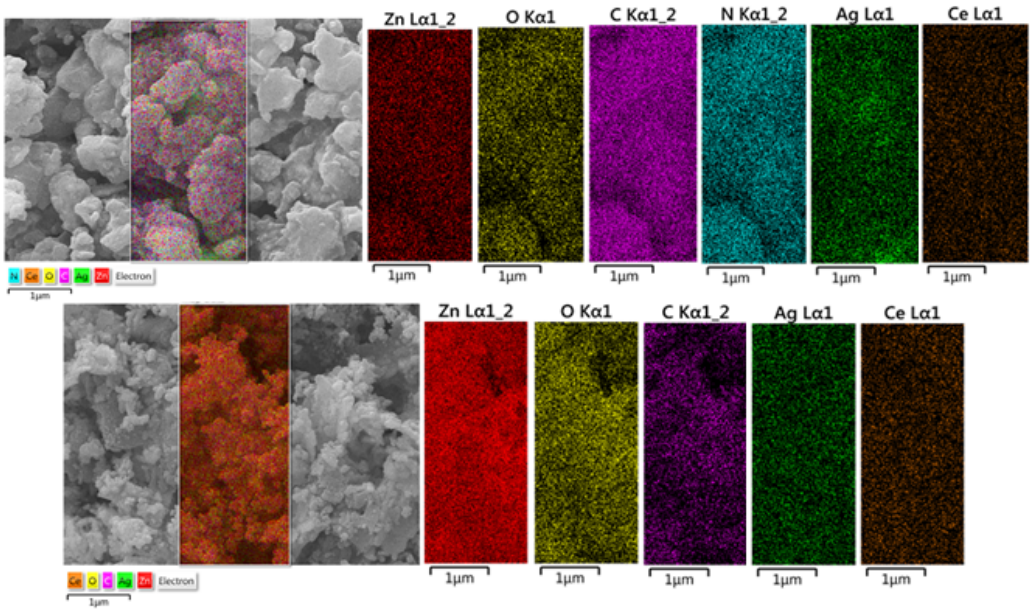

Figure 6. Elemental mapping related to the Ag-Ce-ZnO/PANI and Ag-Ce-ZnO/rGO nanocomposite.

all through the surface.

3.3 UV–Vis spectroscopy

The optical properties belonging to ZnO, PANI, rGO, Ag-Ce-ZnO, Ag-Ce-ZnO/PANI, and Ag-Ce-ZnO/rGO nanocomposites were measured using a double beam spectrometer within the wavelength range 250–700 nm. The samples optical absorption spectra at room temperature can be seen in Fig. 6. The absorption at 370 nm affirmed the highly crystalline structure of ZnO (Fig. 7a). The pure PANI UV–Vis spectrum (Fig. 7b) showed an absorption peak around 377 nm, thus illuminating π- π * electron orbital transition along the given PANI chain, as well as a shoulder at 445 nm; this was for the polaronic transition (polaron- π *) that was created through protonation [28]. For the pure rGO (Fig. 7c), the highest absorption peak at 265 nm relied on the π-plasmon of graphite structure excitation [27].

The spectra, thus, showed that the absorbance intensity of Ag-Ce-ZnO, Ag-Ce-ZnO/PANI, and Ag-Ce-ZnO/rGO (Fig. 8d–f) had been raised in the visible-light region. By contrast, a redshift similar to the previous reports happened [29–31]. The redshift and enhanced absorption could be attributed to the additional energy levels resulting from Ag/Ce doping and the embedment of Ag/Ce ions into the ZnO lattice sites [32]. Ag-Ce-ZnO/PANI nanocomposite can well absorb visible light, in addition to the UV spectrum. This could be related to the interactions existing between PANI chains and Ag-Ce-ZnO nanoparticles, facilitating the charge transfer from PANI to Ag-Ce-ZnO through hydrogen bonding [33]. The redshift in the Ag-Ce-ZnO/rGO nanocomposites' optical absorbance edge, in comparison with zinc oxide, referred to some chemical interaction between Ag-Ce-ZnO semiconductor and rGO. The existence of redshift could be related to the narrowing of the band gap energy in the prepared nanocomposites. A synergistic property was

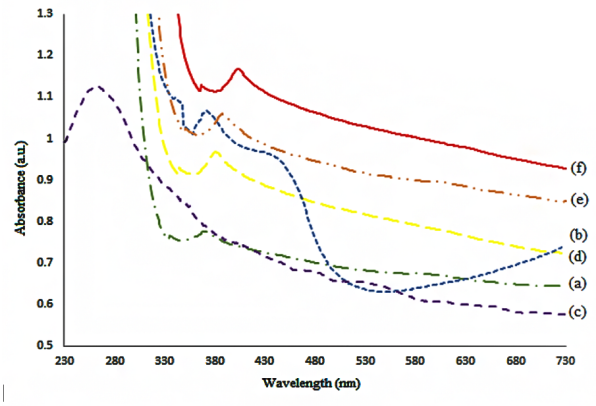

Figure 7. UV–Vis spectra of (a) ZnO, (b) PANI, (c) rGO, (d) Ag-Ce-ZnO, (e)Ag-Ce-ZnO-PANI, and (f) Ag-Ce-ZnO-rGO.

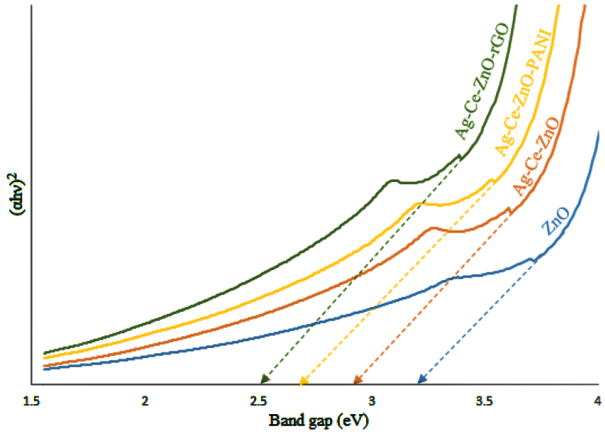

Figure 8. Bandgap plots of ZnO, Ag-Ce-ZnO, Ag-Ce-ZnO/PANI, and Ag-Ce-ZnO/rGO.

created by forming some joint electronic system between rGO and ZnO [34].

The components' optical band gaps were surveyed by applying the UV-Vis absorption spectra by utilizing Tauc's formula (Equation 4) [35].

$$\alpha h\nu = A(h\nu - E_g)^{n/2} \quad (4)$$

, where E_g is related to the energy gap or bandgap, his Planck's constant and ν is frequency, and α refers to the absorption unit, n=1/2, for the direct bandgap materials. The displayed graph, which is plotted between $(\alpha h\nu)^2$ and $h\nu$, represents the optical bandgap, as can be seen in Fig. 8 The band gaps of ZnO, Ag-Ce-ZnO, Ag-Ce-ZnO-PANI, and Ag-Ce-ZnO-rGO were estimated to be 3.1 eV, 2.9 eV, and 3.9 eV, respectively. According to the results, there was a detectable reduction in the bandgap energy of the Ag-Ce-ZnO-rGO nanocomposite in front of other components.

3.4 BET

Surface area plays an imperative role in characterizing the capability of a catalyst, it represents the catalyst's ability to absorb contaminants [36]. As can be seen in Fig. 9 (a-c), the surface area belonging to ZnO, Ag-Ce-ZnO-PANI and Ag-Ce-ZnO-rGO composites was measured amid nitrogen adsorption-desorption isotherms. The N_2 adsorption-desorption isotherms created for the samples were of type IV with an H_3 hysteresis loop, thus affirming that the composite encompassed a mesoporous pore structure. The ZnO Ag-Ce-ZnO-PANI, and Ag-Ce-ZnO-rGO specific surface area was 6.3 $m^2.g^{-1}$, 6.8 $m^2.g^{-1}$, and 15.9 $m^2.g^{-1}$, respectively. The BET-specific surface area of the Ag-Ce-ZnO-rGO composite was much higher in comparison to other samples. It implied the endless specific surface area could give more active sites, making the movement of charge carriers simpler and emphasizing the surprisingly valuable improvement of the photocatalytic capability [37].

3.5 Photocatalytic activity

The photocatalytic properties of the obtained samples were assessed by degrading MG and PNP as the pollutant models. The efficiency of the photocatalytic degradation was measured according to the MG/ PNP solution absorbance via the UV-Vis spectrometer from 0 to 120 minutes on the surface of the catalyst. Fig. 10 (I) and Fig. 11 (I) demonstrate the photocatalytic degradation related to the MG and PNP dye solutions with the irradiation time (a) without catalyst, (b) ZnO, (c) Ag-Ce-ZnO, (d) Ag-Ce-ZnO/PANI, and (e) Ag-Ce-ZnO/rGO, respectively. Remarkably, as shown, Ag-Ce-ZnO/rGO exhibited superior catalytic efficiencies in comparison to other structures in terms of degrading MG

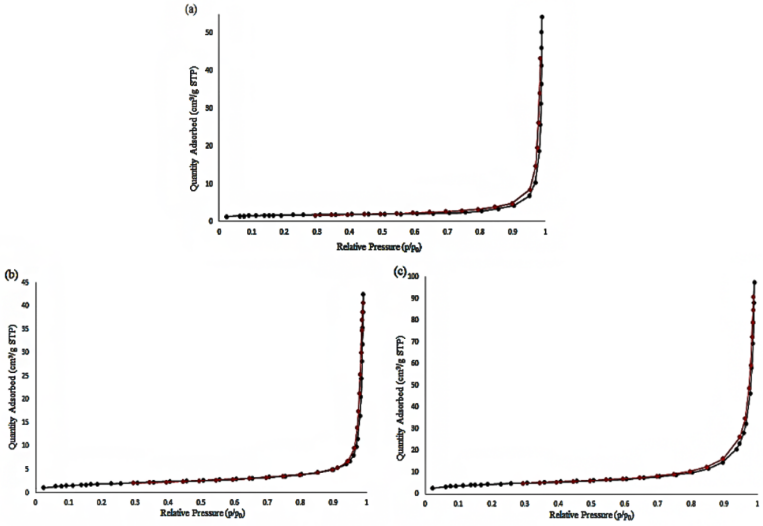

Figure 9. Nitrogen adsorption-desorption data for (a) ZnO, (b) Ag-Ce-ZnO/PANI and (c) Ag-Ce ZnO/rGO.

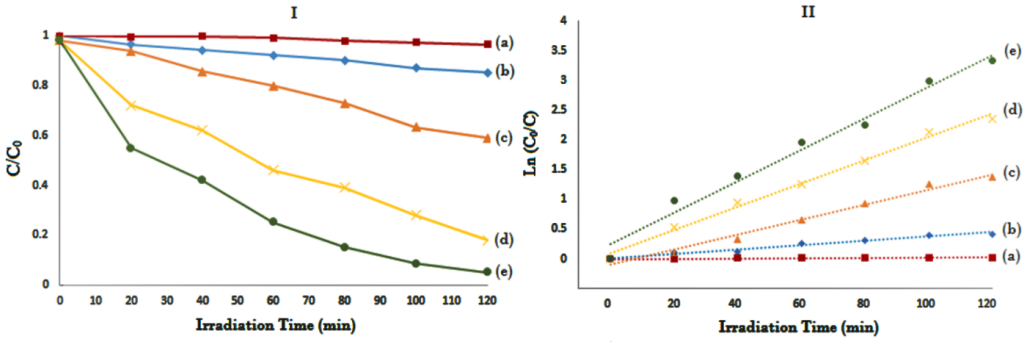

Figure 10. (I) Photocatalytic activity and (II) kinetics study of MG degradation (a) without catalyst, (b) ZnO, (c) Ag-Ce-ZnO, (d) Ag-Ce-ZnO/PANI and (e) Ag-Ce-ZnO/rGO.

and PNP. Under visible light illumination, without a photocatalyst, some negligible degradation was observed and the pure ZnO photocatalyst could decompose 18% of MG and 22% of PNP following the 120 min irradiation time. Behind the 120 min irradiation time, 34%/ 38.2%, 83%/ 89%, and 92%/ 98% of MG/ PNP were decomposed for the samples Ag-Ce-ZnO, Ag-Ce-ZnO/PANI and Ag-Ce-ZnO/rGO, respectively. It should be included that the co-doping of the Ag and Ce to the nanocomposites improved the results obtained from the refined degradation.

As can be seen in Fig. 10 (II) and Fig. 11 (II), the MG and PNP photocatalytic degradation kinetics under visible irradiation were according to the pseudo-first-order kinetic model; this is represented as [38] (Equation 5):

$$\ln\left(\frac{C_0}{C}\right) = k_{app}t \tag{5}$$

The photodegradation rate consistent, k_{app}, which refers to the slope found by the linear fit of ln (C_0/C) vs the irradiation time graph of the kinetic plot, gives some qualitative general appraisal of how viably a dye could be degraded when visible light is present and the use is made of an assisted photocatalyst.

To make a comparison, rate constants (k_{app}), regression coefficient (R^2), and degradation efficiencies (X) of ZnO, Ag-Ce-ZnO, Ag-Ce-ZnO/PANI, and Ag-Ce-ZnO/rGO for degrading MG and PNP can be seen in Table 2. According to the collected results in Table 2, the larger values of rate constant for Ag-Ce-ZnO/rGO could affirm their superior photocatalytic activity; therefore, Ag-Ce-ZnO/rGO could be regarded as the finest photocatalyst in the degradation of the MG and PNP. The presence of rGO in the synthesized nanocomposite will improve the electron transfer between the catalyst and the pollutants. The maximum photocatalytic activity of the Ag-Ce-ZnO/rGO nanocomposite could be explained by the improved charge separation and greater specific surface area, as well as more active sites for photocatalysis. Also, the Ag-Ce-ZnO/PANI sample possesses higher photocatalytic capability in comparison to ZnO and Ag-Ce-ZnO, contributing to considerable conductivity, special optical and electrical properties, and the composite small particles.

3.6 Scavenger test

The primary reactive oxygen species (ROS) in the photocatalytic degradation of toxic dyes were monitored using radical trapping studies to comprehend the photocatalytic mechanism [39]. Distinct scavengers, isopropanol (IPA), 1,4 benzoquinone (BQ) [40] , and Ethylene Diamine Tetra Acetic Acid (EDTA) [41] as yielding scavengers for hydroxyl radical ($OH^{\bullet}$), superoxide radical ($O_2^{\bullet -}$), and hole (h^+) employed in photocatalytic study for both dyes. According to the results obtained from fig. 12, it can be seen that all three active species play an important role in the activity of photocatalytic degradation. also conducted a control experiment without any radical scavengers to rule out the potential of color deterioration caused by radical scavengers. absence of any scavenger shows no obvious change occurred during the degradation experiment process [42].

3.7 Mechanism of photocatalytic degradation

To probe the mechanism of photocatalytic degradation, we initiated the determination of the position of the conductivity bands and the capacity of zinc oxide. The valence band (VB) and conduction band (CB) potential of a semiconductor can be theoretically calculated using Mulliken electronegativity

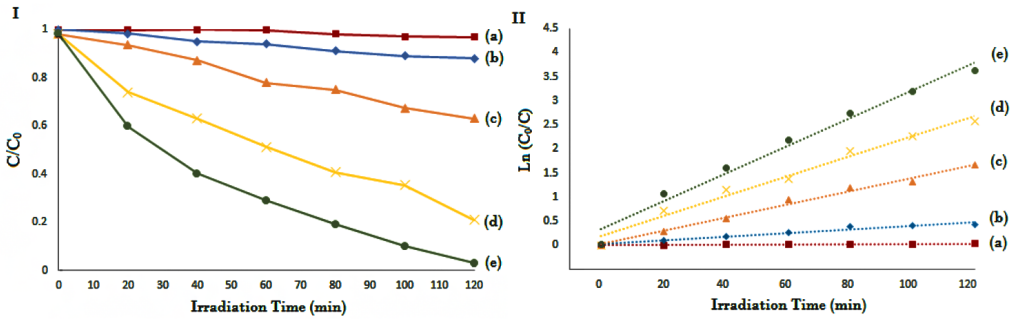

Figure 11. (I) Photocatalytic activity and (II) kinetics study of PNP degradation (a) without catalyst, (b) ZnO, (c) Ag-Ce-ZnO, (d) Ag-Ce-ZnO/PANI and (e) Ag-Ce-ZnO/rGO.

Table 2. Photocatalytic degradation results of MG and PNP 120 min of visible light irradiation.

photocatalyst	**k_{app} (min^{-1})**		**R^2**		**degradation efficiencies**	
	MG	PNP	MG	PNP	MG	PNP
without catalyst	0.0002	0.0003	0.9816	0.9869	5	6
ZnO	0.0036	0.0038	0.9766	0.9516	18	22
Ag-Ce-ZnO	0.0126	0.0138	0.9829	0.9887	48	53
Ag-Ce-ZnO/PANI	0.0196	0.0207	0.993	0.9807	83	89
Ag-Ce-ZnO/rGO	0.0265	0.0289	0.9802	0.9803	92	98

and the bandgap of a semiconductor by the following:

$$E_{VB} = \chi - E_e + 0.5E_g \quad (6)$$

$$E_{CB} = E_{VB} - E_g \quad (7)$$

where E_{VB} and E_{CB} are the top of the valence band and the bottom of the conduction band of the semiconductor, E_g is the band gap energy, and E_e is the energy of free electrons on the hydrogen scale with a fixed value of 4.5 eV vs. NHE, and χ is the geometric mean of the Mulliken electronegativity of the constituent atoms in the semiconductor. The Mulliken electronegativity of an atom is the arithmetic mean of the first ionization energy and the first electron affinity. The detailed calculation steps for obtaining the Valence band and Conduction band of ZnO were illustrated as follows:
The first ionization energy of silver element (Zn): I_1 = 906.4 kj.mol^{-1}
The first electron affinity of silver element (Zn): E_1 = - 60 kj.mol^{-1}
The Mulliken electronegativity of silver element (Zn):

$$\chi = \frac{1}{2}(I_1 + E_1) = \frac{1}{2}(906.4 - 60) = 423.2 \text{ kj.mol}^{-1} \quad (8)$$

Because: 1 eV = 1.6022×10^{-19} C×1 V = 1.6022×10^{-19} J. And the Avogadro constant (NA) = 6.022× 10^{23} mol^{-1}.
Thus, the Mulliken electronegativity of a zinc atom (Zn) can be calculated as follows:

$$\begin{aligned}\chi_{Ag} &= 423.2 \times 10^3 \text{J.mol}^{-1} \\ &\div (6.022 \times 10^{23} \text{mol}^{-1}) \\ &\div (1.6022 \times 10^{-19} \text{J}) \\ &= 4.386\end{aligned} \quad (9)$$

For oxygen (O):
I_1 = 1313.9 kj.mol^{-1}
E_1 = 141 kj.mol^{-1},

$$\begin{aligned}\chi &= \frac{1}{2}(I_1 + E_1) = \frac{1}{2}(1313.9 + 141) \\ &= 727.45 \text{ kj.mol}^{-1}\end{aligned} \quad (10)$$

Thus, the Mulliken electronegativity of an iodine atom (O) is calculated as follows:

$$\begin{aligned}\chi_0 &= 727.45 \times 10^3 \text{J.mol}^{-1} \\ &\div (6.022 \times 10^{23} \text{mol}^{-1}) \\ &\div (1.6022 \times 10^{-19} \text{J}) \\ &= 7.539\end{aligned} \quad (11)$$

The geometric mean of the Mulliken electronegativity for ZnO (χ) is calculated as follows:

$$\chi = \sqrt{\chi_{Zn} \cdot \chi_0} = \sqrt{4.386 \times 7.539} = 5.75 \quad (12)$$

The bandgap (E_g) of ZnO was obtained by the UV-visible diffuse reflectance measurement and was determined to be 3.3 eV (Fig. 12), Therefore, The Valence band of ZnO is calculated as follows:

$$E_{VB} = X - E_e + 0.5E_g = 5.75 - 4.5 + 0.5 \times 3.3 = 2.9\,V \quad (13)$$

The conduction band of ZnO is calculated as follows:

$$E_{CB} = E_{VB} - E_g = 2.9 - 3.3 = -0.4\,V \quad (14)$$

[44], based on the experimental results we proposed a charge transfer mechanism forAg-CeZnO-rGO heterojunction as described schematically in Fig. 13 The work function of bulk Ag and Ce are 4.26 [47] and 2.9 eV [48], respectively. At the same time, the work function of ZnO single crystal is near 4.7 eV [48]. The n-type doping of ZnO NPs with the number of defects on the surface leads the Fermi level to move towards CB. Therefore, an Ohmic contact between ZnO with Ag and Ce would be formed After contacting, the Fermi level of metal NPs will be equal to that of ZnO The ohmic contact will lead to the band bent downwards, giving rise to a barrier-less electron transfer from ZnO phase to the metals phase. Moreover, it drives the photogenerated holes migrating into the bulk of ZnO, thus the charge separation efficiency is enhanced It should also be mentioned that graphene helps to increase the efficiency of photocatalytic degradation by facilitating the electron

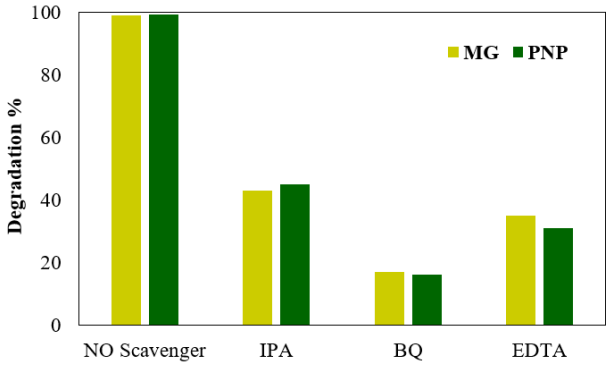

Figure 12. Effects of different scavengers on the photodegradation of MG and PNP.

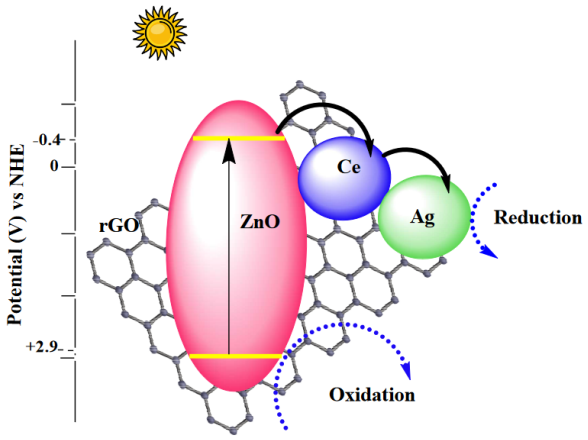

Figure 13. Schematic illustration of the probable photocatalytic mechanism of Ag-Ce-ZnO/rGO nanocomposite.

Table 3. Comparison of different ZnO-based photocatalysts.

photocatalyst	light	dye	degradation%	time (min)	ref
Ag-Cu-ZnO	vis	MB	95	180	[43]
WO_3/NiO/ZnO	sun	MB	45.87	105	[44]
$(CoFe_2O_4)_{0.5}/Ag_2S$-ZnO	vis	MB	99	240	[45]
$ZnO/ZnFe_2O_4/TiO_2$	vis	MO	96.32	150	[46]
Ag-Ce-ZnO/PANI	vis	MG PNP	89 83	120	this work
Ag-Ce-ZnO/rGO	vis	MG PNP	98 92	120	this work

transfer path [40, 48].

In addition, a comparison study based on different ZnO-based photocatalysts is given in Table. 3.

Recovery and reuse of photocatalyst are imperative from economic aspects. The reusability of the synthesized composites is detailed in Fig. 14, representing cycling runs within the photocatalytic degradation of MG and PNP in the presence of Ag-Ce-ZnO/rGO beneath the visible light irradiation. As it is evident, amid the 120 min, the photodegradation rate of MG/ PNP was picked up to be 99.8/ 99.2, 98.9/ 98.5, 98.1/ 97.7, 97.6/ 97.2 and 96.4/ 95.8 % for the primary, moment, third, fourth and fifth cycles, respectively. The slight decrease in photoactivity observed after reusing the Ag-Ce-ZnO/PANI and rGO samples may be due to factors such as material degradation, surface contamination, structural changes, loss of active sites, and particle aggregation. These factors could collectively contribute to the deviation in photocatalytic performance.

4. Conclusion

To conclude, ZnO, Ag-Ce-ZnO, Ag-Ce-ZnO/PANI, and Ag-Ce-ZnO/rGO samples were effectively manufactured through precipitation and polymerized during in-situ polymerization. The prepared samples' properties were characterized by different strategies. The photocatalytic activity of the samples was studied through degrading MG and PNP dye under visible light irradiation. According to the obtained findings, there was a drastic improvement in the photocatalytic activity of the Ag-Ce-ZnO/rGO nanocomposite. this improved photodegradation was majorly due to the increased specific surface area of this novel nanocomposite which helped with absorbing more contaminants. Of course, the delayed rate of the charge recombination, extraordinary adsorption of dyes, stronger visible light absorption, and quick transfer processes were effective as well. This synthesized nanocomposite had the capability to be reused for five progressive runs without significant change in its photodegradation ability which is an advantage regarding its environmentally friendly behavior.

Acknowledgement

The authors are grateful to K.N. Toosi University of Technology for the help to undertake the work.

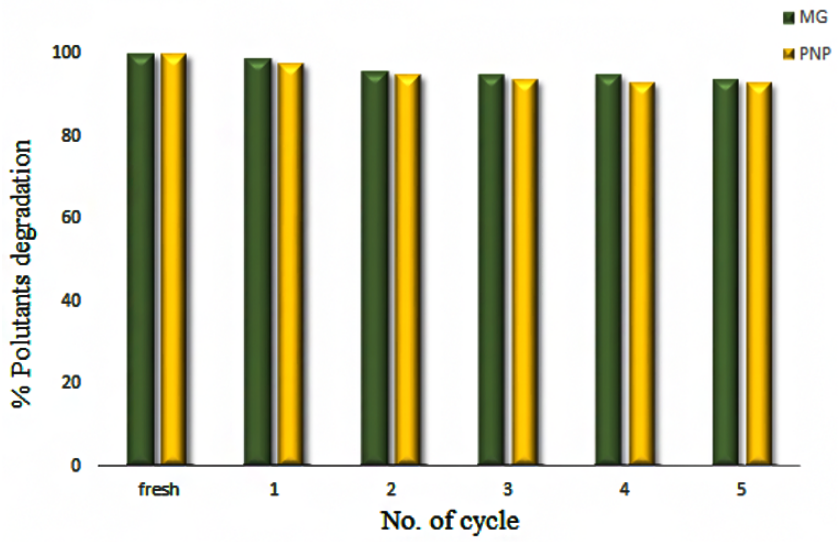

Figure 14. Reusability study Ag-Ce-ZnO/rGO nanocomposite.

Authors Contributions
All authors have contributed equally to prepare the paper.

Availability of Data and Materials
The data that support the findings of this study are available from the corresponding author upon reasonable request.

Conflict of Interests
The authors declare that they have no known competing financial interests or personal relationships that could have appeared to influence the work reported in this paper.

References

[1] S.G. Kumar and K.K. Rao. Zinc oxide based photocatalysis: Tailoring surface-bulk structure and related interfacial charge carrier dynamics for better environmental applications. *RSC Adv*, **5**(2015):3306–3351, . DOI: https://doi.org/10.1039/C4RA13299H.

[2] F.J.A. Villaluz, M.D.G de Luna, J.I. Colades, S. Garcia-Segura, and M.C. Lu. Removal of 4-chlorophenol by visible-light photocatalysis using ammonium iron (ii) sulfate-doped nano-titania. *Process Saf. Environ. Prot*, **125**(2019):121–128. DOI: https://doi.org/10.1016/j.psep.2019.03.001.

[3] M.A. Al-Nuaim, A.A. Alwasiti, and Z.Y. Shnain. The photocatalytic process in the treatment of polluted water. *Chem. Pap*, **77**(2023):677–701. DOI: https://doi.org/10.1007/s11696-022-02468-7.

[4] N. Ahmad, J. Anae, M.Z. Khan, S. Sabir, X.J. Yang, V.K. Thakur, and F. Coulon. Visible light-conducting polymer nanocomposites as efficient photocatalysts for the treatment of organic pollutants in wastewater. *Enviro Manage*, **295**(2021):113362, . DOI: https://doi.org/10.1016/j.jenvman.2021.113362.

[5] S. Raha and M. Ahmaruzzaman. Zno nanostructured materials and their potential applications: progress, challenges and perspectives. *Nanoscale Adv*, **4**(2022):1868–1925. DOI: https://doi.org/10.1039/D1NA00880C.

[6] S.G. Kumar and K.K. Rao. Zinc oxide based photocatalysis: Tailoring surface-bulk structure and related interfacial charge carrier dynamics for better environmental applications. *RSC Adv*, **5**(2015):3306–3351, . DOI: https://doi.org/10.1039/C4RA13299H.

[7] M. Wang, F. Ren, J. Zhou, G. Cai, L. Cai, Y. Hu, and S. Shen. N doping to zno nanorods for photoelectrochemical water splitting under visible light: engineered impurity distribution and terraced band structure. *Sci. Rep*, **5**(2015):12925, . DOI: https://doi.org/10.1038/srep12925.

[8] F. Heshmatpour and M.S. Abdikhani. Ce-ag-zno/fe_3o_4 nanocomposites: A novel magnetically separable photocatalyst for highly efficient photodegradation of contaminants. *Physica B Condens. Matter*, **570**(2019):312–319. DOI: https://doi.org/10.1016/j.physb.2019.06.005.

[9] K. Pandiselvi, H. Fang, X. Huang, J. Wang, X. Xu, and T. Li. Constructing a novel carbon nitride/polyaniline/zno ternary heterostructure with enhanced photocatalytic performance using exfoliated carbon nitride nanosheets as supports. *Hazard. Mater*, **314**(2016):67–77. DOI: https://doi.org/10.1016/j.jhazmat.2016.04.035.

[10] S. Rabieh, K. Nassimi, and M. Bagheri. Synthesis of hierarchical zno–reduced graphene oxide nanocomposites with enhanced adsorption–photocatalytic performance. *Mater. Lett*, **162**(2016):28–31. DOI: https://doi.org/10.1016/j.matlet.2015.09.111.

[11] R. Kumar, A. Sudhaik, P. Raizada, V.H. Nguyen, Q. Van Le, T. Ahamad, and P. Singh. Integrating k and p co-doped g-c_3n_4 with $znfe_2o_4$ and graphene oxide for s-scheme-based enhanced adsorption coupled photocatalytic real wastewater treatment. *Chemosphere*, **337**(2023):139267, . DOI: https://doi.org/10.1016/j.chemosphere.2023.139267.

[12] A. Kumar, S. Billa, S. Chaudhary, A.B.V. Kiran Kumar, Ch.V.V. Ramana, and D. Kim. Ternary nanocomposite for solar light photocatalyic degradation of methyl orange. *Inorg. Chem. Commun*, **97**(2018):191–195, . DOI: https://doi.org/10.1016/j.inoche.2018.09.038.

[13] A. Habibi-Yangjeh and M. Shekofteh-Gohari. Synthesis of magnetically recoverable visible-light-induced photocatalysts by combination of fe_3o_4/zno with bioi and polyaniline. *Prog. Nat. Sci.: Mater. Int*, **29**(2019):145–155. DOI: https://doi.org/10.1016/j.pnsc.2019.03.003.

[14] R. Saravanan, E. Sacari, F. Gracia, M.M. Khan, E. Mosquera, and V.K. Gupta. Conducting pani stimulated zno system for visible light photocatalytic degradation of coloured dyes. *Mol. Liq*, **221**(2016):1029–1033, . DOI: https://doi.org/10.1016/j.molliq.2016.06.074.

[15] S.A. Carminati, I. Rodríguez-Gutiérrez, A. de Morais, B.L. da Silva, M.A. Melo, F.L. Souza, and A.F. Nogueira. Challenges and prospects about the graphene role in the design of photoelectrodes for sunlight-driven water splitting. *RSC Adv*, **11**(2021):14374–14398. DOI: https://doi.org/10.1039/D0RA10176A.

[16] G.S. Shanker, A. Biswas, and S. Ogale. 2d materials and their heterostructures for photocatalytic water splitting and conversion of co_2 to value chemicals and fuels. *phys. energy*, **3**(2021):022003. DOI: https://doi.org/10.1088/2515-7655/abdcab.

[17] M.J. Chatterjee, S.T. Ahamed, M. Mitra, Ch. Kulsi, A. Mondal, and D. Banerjee. Visible-light influenced photocatalytic activity of polyaniline-bismuth selenide composites for the degradation of methyl orange, rhodamine b and malachite green dyes. *Appl. Surf. Sci*, **470**(2019):472–483. DOI: https://doi.org/10.1016/j.apsusc.2018.11.085.

[18] V. Vaiano, M. Matarangolo, J.J. Murcia, H. Rojas, J.A. Navio, and M.C. Hidalgo. Enhanced photocatalytic removal of phenol from aqueous solutions using zno modified with ag. *Appl. Catal. B*, **225**(2018):197–206. DOI: https://doi.org/10.1016/j.apcatb.2017.11.075.

[19] L. Soto-Vázquez, M. Cotto, C. Morant, J. Duconge, and F. Marquez. Facile synthesis of zno nanoparticles and its photocatalytic activity in the degradation of 2-phenylbenzimidazole-5-sulfonic acid. *Photochem. Photobiol. A*, **332**(2017):331–336. DOI: https://doi.org/10.1016/j.jphotochem.2016.09.010.

[20] W. Ding, L. Zhao, H. Yan, X. Wang, X. Liu, X. Zhang, and B. Tang. Bovine serum albumin assisted synthesis of ag/ag_2o/zno photocatalyst with enhanced photocatalytic activity under visible light. *Colloids Surf. A*, **568**(2019):131–140. DOI: https://doi.org/10.1016/j.colsurfa.2019.02.015.

[21] M. Ahmad, E. Ahmed, F. Zafar, N.R. Khalid, N.A. Niaz, A. Hafeez, and H.O.N.G. Zhanglian. Enhanced photocatalytic activity of ce-doped zno nanopowders synthesized by combustion method. *Rare Earths*, **33**(2015):255–262, . DOI: https://doi.org/10.1016/S1002-0721(14)60412-9.

[22] H. Wu, S. Lin, C. Chen, W. Liang, X. Liu, and H. Yang. A new zno/rgo/polyaniline ternary nanocomposite as photocatalyst with improved photocatalytic activity. *Mater. Res. Bull*, **83**(2016):434–441. DOI: https://doi.org/10.1016/j.materresbull.2016.06.036.

[23] R. Nosrati, A. Olad, and R. Maramifar. Degradation of ampicillin antibiotic in aqueous solution by zno/polyaniline nanocomposite as photocatalyst under sunlight irradiation. *Environ. Sci. Pollut. Res*, **19**(2012):2291–2299. DOI: https://doi.org/10.1007/s11356-011-0736-5.

[24] H. Wang, D. Peng, T. Chen, Y. Chang, and Sh. Dong. A novel photocatalyst agbr/zno/rgo with high visible light photocatalytic activity. *Ceram. Int*, **42**(2016):4406–4412, . DOI: https://doi.org/10.1016/j.ceramint.2015.11.124.

[25] M. Rostami. Photodecomposition and adsorption of hazardous organic pollutants by ce-doped zno@ ce-doped tio_2-n/s-dual doped rgo ternary nanocomposites photocatalyst for water remediation. *Mol. Struct*, **1185**(2019):191–199. URL 10.1016/j.molstruc.2019.02.094.

[26] M. Bansal, D. S. Ahlawat, A. Singh, V. Kumar, and S. P. Ratheei. Effect of heat treatment on the microstructural properties of silica embedded cobalt ferrite nanocomposites. *Nanocomposites*, **6**(2020):158–164. DOI: https://doi.org/10.1080/20550324.2020.1865711.

[27] R.F. Albers, R.A. Bini, J.B. Souza, Jr.D.T. Machado, and L.C. Varanda. A general one-pot synthetic strategy to reduced graphene oxide (rgo) and rgo-nanoparticle hybrid materials. *Carbon*, **143**(2019):73–84. DOI: https://doi.org/10.1016/j.carbon.2018.10.087.

[28] M. Mitra, A. Ghosh, A. Mondal, K. Kargupta, S. Ganguly, and D. Banerjee. Facile synthesis of aluminium doped zinc oxide-polyaniline hybrids for photoluminescence and enhanced visible-light assisted photo-degradation of organic contaminants. *Appl. Surf. Sci*, **402**(2017):418–428. DOI: https://doi.org/10.1016/j.apsusc.2017.01.072.

[29] S. Vignesh, S. Suganthi, J.K. Sundar, V. Raj, and P.R.I Devi. Highly efficient visible light photocatalytic and antibacterial performance of pvp capped cd: Ag: Zno photocatalyst nanocomposites. *Appl. Surf. Sci*, **479**(2019):914–929. DOI: https://doi.org/10.1016/j.apsusc.2019.02.064.

[30] M. Ahmad, E. Ahmed, Z.L. Hong, N.R. Khalid, W. Ahmed, and A. Elhissi. Graphene–ag/zno nanocomposites as high performance photocatalysts under visible light irradiation. *Alloys Compd*, **557**(2013):717–727, . DOI: https://doi.org/10.1016/j.jallcom.2013.06.137.

[31] R. Saravanan, E. Sacari, F. Gracia, M. Mansoob Khan, E. Mosquera, and V.K. Gupta. Conducting pani stimulated zno system for visible light photocatalytic degradation of coloured dyes. *Mol. Liq*, **221**(2016):1029–1033, . DOI: https://doi.org/10.1016/j.molliq.2016.06.074.

[32] J. Lang, J. Wang, Q. Zhang, X. Li, Q. Han, M. Wei, Y. Sui, D. Wang, and J. Yang. Chemical precipitation synthesis and significant enhancement in photocatalytic activity of ce-doped zno nanoparticles. *Ceram. Int*, **42**(2016):14175–14181. DOI: https://doi.org/10.1016/j.ceramint.2016.06.042.

[33] E. Asgari, A. Esrafili, A. Jonidi Jafari, R. Rezaei Kalantary, H. Nourmoradi, and M. Farzadkia. The comparison of zno/polyaniline nanocomposite under uv and visible radiations for decomposition of metronidazole: degradation rate, mechanism and mineralization. *Process Saf. Environ. Prot*, **12**(2019):65–76. DOI: https://doi.org/10.1016/j.psep.2019.05.050.

[34] K. Huang, Y.H. Li, S. Lin, C. Liang, H. Wang, C.X. Ye, Y.J. Wang, R. Zhang, D.Y. Fan, H.J. Yang, Y.G. Wang, and M. Lei. A facile route to reduced graphene oxide–zinc oxide nanorod composites with enhanced photocatalytic activity. *Powder Technol*, **257**(2014):113–119. DOI: https://doi.org/10.1016/j.powtec.2014.02.047.

[35] X. Wang, X. Wan, X. Xu, and X. Chen. Facile fabrication of highly efficient agi/zno heterojunction and its application of methylene blue and rhodamine b solutions degradation under natural sunlight. *Appl. Surf. Sci*, **321**(2014):10–18, . DOI: https://doi.org/10.1016/j.apsusc.2014.09.103.

[36] M. Chandrasekhar, H. Nagabhushana, Y.S. Vidya, K.S. Anantharaju, S.C. Sharma, H.B. Premkumar, S.C. Prashantha, B. Daruka Prasad, C. Shivakumara, R. Saraf, and H.P.Nagaswarupa. Synthesis of eu^{3+}-activated zno superstructures: Photoluminescence, judd–ofelt analysis and sunlight photocatalytic properties. *Mol. Catal. A: Chem*, **409**(2015):26–41. DOI: https://doi.org/10.1016/j.molcata.2015.08.002.

[37] L. Zhang, N. Li, H. Jiu, G. Qi, and Y.Huang. Zno-reduced graphene oxide nanocomposites as efficient photocatalysts for photocatalytic reduction of co_2. *Ceram. Int*, **41**(2015):6256–6262, . DOI: https://doi.org/10.1016/j.ceramint.2015.01.044.

[38] M. Sabri, A. Habibi-Yangjeh, and S. Ghosh. Novel zno/$cubi_2o_4$ heterostructures for persulfate-assisted photocatalytic degradation of dye contaminants under visible light. *Photochem. Photobiol. A*, **391**(2020):112397. DOI: https://doi.org/10.1016/j.jphotochem.2020.112397.

[39] K. Sharma, V. Hasija, M. Malhotra, P.K. Verma, A.A.P. Khan, S. Thakur, and P. Raizada. A review of cds-based s-scheme for photocatalytic water splitting: synthetic strategy and identification techniques. *Int. J. Hydrogen Energy*, **52**(2024):804–818. DOI: https://doi.org/10.1016/j.ijhydene.2023.09.033.

[40] A.A.P. Khan, A. Sudhaik, P. Raizada, A. Khan, M.A. Rub, N. Azum, and A.M. Asiri. Agi coupled sio_2@ $cufe_2o_4$ novel photocatalytic nano-material for photo-degradation of organic dyes. *Catal. Commun*, **179**(2023):106685. DOI: https://doi.org/10.1016/j.catcom.2023.106685.

[41] C. Yavuz and S. Erten-Ela. Solar light-responsive α-fe_2o_3/cds/g-c_3n_4 ternary photocatalyst for photocatalytic hydrogen production and photodegradation of methylene blue. *Alloys Compd*, **908**(2022):164584. DOI: https://doi.org/10.1016/j.jallcom.2022.164584.

[42] M. Malhotra, A. Sudhaik, P. Raizada, T. Ahamad, N.H. Nguyen, Q. Van Le, and P. Singh. An overview on cellulose-supported photocatalytic materials for the efficient removal of toxic dyes. *Ind Crops Prod*, **202**(2023):117000. DOI: https://doi.org/10.1016/j.indcrop.2023.117000.

[43] M. Rabbani, J. Shokraiyan, R. Rahimi, and R. Amrollahi. Comparison of photocatalytic activity of zno, ag-zno, cu-zno, ag, cu-zno and tpps/zno for the degradation of methylene blue under uv and visible light irradiation. *Water Sci. Technol*, **84**(2021):1813–1825. DOI: https://doi.org/10.2166/wst.2021.360.

[44] H.M. Abo-Dief, O.K. Hussein, A. Ihsan, S.M. El-Bahy, A.M. Raslan, M. Shahid, and M.F. Warsi. Ternary metal oxide wo_3. nio. zno nanoparticles and their composite with cnts for organic dye photocatalytic degradation. *Ceram. Int*, **48**(2022):22269–22277. DOI: https://doi.org/10.1016/j.ceramint.2022.04.225.

[45] E.O. Ichipi, A.B. Mapossa, A.C.F. Costa, E.M. Chirwa, and S.M. Tichapondwa. Fabrication and characterization of recyclable, magnetic ($cofe_2o_4$) x/ag_2s-zno composites for visible-light-induced photocatalytic degradation of methylene blue dye. *Water Process. Eng*, **54**(2023):104040. DOI: https://doi.org/10.1016/j.jwpe.2023.104040.

[46] J. Zhang, M. Kuang, Y. Cao, and Z. Ji. Environment-friendly ternary zno/$znfe_2o_4$/tio_2 composite photocatalyst with synergistic enhanced photocatalytic activity under visible-light irradiation. *Solid State Sci*, **129**(2022):106913, . DOI: https://doi.org/10.1016/j.solidstatesciences.2022.106913.

[47] Q. Liu, Z. Wang, H. Chen, H.Y. Wang, H. Song, J. Ye, and Y. Weng. Rules for selecting metal cocatalyst based on charge transfer and separation efficiency between zno nanoparticles and noble metal cocatalyst ag/au/pt. *Chem Cat Chem*, **12**(202):3838–3842. DOI: https://doi.org/10.1002/cctc.202000280.

[48] M. M. Hasan, E. Kisi, and H. Sugo. Single-step low-temperature synthesis routes for (ba, ce, gd) hexaborides and their thermionic emission properties. *Alloys Compd*, **916**(2022):165474. DOI: https://doi.org/10.1016/j.jallcom.2022.165474.